

CO₂ Electroreduction to CO Over Silver Nanoclusters: The Impact of Nuclearity on Synergistic Activity Modulation

Parvathy Jayan, Arijit Jana, Zhengyuan Li, Rahul Kumar Sharma, Vivek Yadav, Astrid Campos Mata, Ming-Hsuan Li, Ali Shayesteh Zeraati, Tomas Base, Sung-Fu Hung, Jingjie Wu, Biswarup Pathak, Thalappil Pradeep, and Soumyabrata Roy*

Electrochemical reduction of CO₂ (eCO₂R) powered by renewable energy holds the potential to produce sustainable platform chemicals and decarbonize the hard-to-abate sectors. Herein, the structure-activity correlation of atomically precise silver nanoclusters (NCs) in eCO₂R to carbon monoxide (CO) is studied, elucidating the effect of the nuclearity of metal core and the electronic nature of the ligands. Electrocatalytic studies on Ag NCs, [Ag₂₁(MCT)₁₂(TPP)₂]⁺, [Ag₃₁(TRZ)₁₀]²⁻, [Ag₄₂(CBDT)₁₅(TPP)₄]²⁻ (shortly, Ag₂₁, Ag₃₁, and Ag₄₂, respectively), reveal that the CO Faradaic efficiency (FE_{CO}) increases while the FE_{CO(max)} (the maximum FE_{CO}) moves to higher positive potentials upon decreasing the nuclearity of these Ag NCs, almost in a quantitative correlation. Notably, every ≈ten Ag atoms variation in the cluster shifts the potentials for FE_{CO(max)} and maximum partial current density, $j_{CO(max)}$ by ≈70 and ≈80 mV, respectively. The smallest nanocluster, Ag₂₁, achieved a near-unity FE_{CO(max)} of 99.6% at −0.59 V vs RHE, and a competitive eCO₂R-to-CO rate, producing a $j_{CO(max)}$ of 148 mA cm^{−2} at −0.7 V vs RHE. First principle calculations reveal that decreasing the atomicity in Ag NCs reduces the activation energy barriers for the 2e[−] reduction pathway due to the modulation of surface charge distribution and the electronic density of states of the active Ag sites.

1. Introduction

Renewable energy (RE) powered electrochemical CO₂ reduction reaction (eCO₂R) offers a promising approach to transform greenhouse gases like CO₂ into valuable products that can close the artificial carbon cycle and store intermittent RE in chemical bonds (C–C, C–H, and C–O bonds).^[1–4] eCO₂R offer significant advantages over other chemical conversion routes, due to its ambient operational conditions, adaptability to renewable energy infrastructure, and the wide product scope comprising C₁–C₃ hydrocarbons, oxygenates, and key commodity chemicals.^[5–11] Among these, CO is a promising eCO₂R product having low thermodynamic potential requirements (−0.1 V vs reversible hydrogen electrode [RHE]), fast kinetics, and ubiquitous applications in the chemical (use as syngas in Fischer-Tropsch process), fertilizer, biorefineries, and metal/steel processing sectors.^[12–18]

P. Jayan, S. Roy
Department of Sustainable Energy Engineering
Indian Institute of Technology Kanpur
Uttar Pradesh 208016, India
E-mail: soumyar@iitk.ac.in

A. Jana, V. Yadav, T. Pradeep
Department of Science and Technology (DST)
Unit of Nanoscience and Thematic Unit of Excellence
Department of Chemistry
Indian Institute of Technology (IIT) Madras
Chennai 600036, India

Z. Li, J. Wu
Department of Chemical and Environmental Engineering
University of Cincinnati
Cincinnati, OH 45221, USA

R. K. Sharma, B. Pathak
Department of Chemistry
Indian Institute of Technology
Indore, Madhya Pradesh 453552, India

A. C. Mata
Department of Materials Science and Nanoengineering
Rice University
Houston, TX 77005, USA

M.-H. Li, S.-F. Hung
Department of Applied Chemistry and Centre for Emergent Functional
Matter Science
National Yang Ming Chiao Tung University
Hsinchu 300, Taiwan

A. Shayesteh Zeraati
Acceleration Consortium
University of Toronto
80 St. George St., Toronto, ON M5S 3H6, Canada

T. Base
Department of Syntheses
Institute of Inorganic Chemistry
The Czech Academy of Sciences
250 68 Husinec-Rez, Prague 25068, Czech Republic

The ORCID identification number(s) for the author(s) of this article can be found under <https://doi.org/10.1002/sml.202505305>

DOI: 10.1002/sml.202505305

Coinage metals viz. Cu, Ag, and Au have shown tremendous potential in $e\text{CO}_2\text{R}$ due to their partially filled d orbitals, which can favorably interact and overlap with the 2p orbitals of carbon to activate CO_2 .^[19,20] Among these, Cu easily stabilizes the CO intermediate, leading to the formation of higher hydrocarbon and multi-electron (beyond $2e^-$) reduced products.^[21] Ag and Au, on the other hand, are highly selective for the production of CO due to the weak binding and easy desorption of CO.^[22–25] Ag is considered more viable due to its cost benefits over Au and has demonstrated its $e\text{CO}_2\text{R}$ -to-CO potential in various nanoengineered forms.^[26–29] CO, a 2-electron reduced $e\text{CO}_2\text{R}$ product, usually forms via a proton-coupled electron transfer process ($\text{CO}_2 + 2\text{H}^+ + 2e^- \rightarrow \text{CO} + \text{H}_2\text{O}$), involving activated $^*\text{COOH}$ as a key intermediate. CO_2 gets adsorbed and activated as $^*\text{CO}_2^-$ intermediate, which on subsequent hydrogenation forms C-bound $^*\text{COOH}$, which is further reduced and eventually desorbs as CO.^[30,31] Activation of CO_2 and formation of $^*\text{COOH}$ can both be rate-limiting steps on Ag/Au catalysts.^[32,33]

Various nanoengineering levers, such as morphology, size, doping/alloying, superstructural assembly, surface modifications, and nano-structuring, have started pushing the boundaries of $e\text{CO}_2\text{R}$ -to-CO production on Ag catalysts.^[34–38] However, achieving near-unity selectivity of $e\text{CO}_2\text{R}$ -to-CO at competitive current densities is challenging, due to high overpotential needed for CO_2 activation and competing hydrogen evolution reaction in aqueous electrolytes.^[33] Moreover, the heterogeneity and dynamic nature of these nanostructures and inconclusive active site configuration impede the development of meaningful and reliable structure-activity correlations.

To that end, ligand (monolayer) stabilized atomically precise metal nanoclusters (MNCs), typically consisting of 4–500 metal atoms with well-defined structures, are an ideal platform for tuning $e\text{CO}_2\text{R}$ activity at the molecular level and elucidating the tunable interface of heterogeneous catalysis.^[39–44] These molecular materials comprising coinage metals are steadily emerging as a unique class of catalysts owing to their high surface area-to-volume ratio, distinct electronic properties, and metal-ligand interactions.^[45,46] Such features can improve the performance by activating reactant molecules on the undercoordinated and charge-modulated surface active sites, steering the pathways and energetics of the redox processes.^[47–49] Further, the quantum confinement effect in MNCs can alter the band gap, which can resonate with the activation energy barriers of the intermediate species.^[50,51] Engineering approaches on Au and Ag NCs are extensively exploring these features to fine-tune and boost their $e\text{CO}_2\text{R}$ -to-CO activity.^[52–56]

For example, in one of the early pioneering studies on thiol-protected Au NC involving $[\text{Au}_{25}(\text{SC}_2\text{H}_4\text{Ph})_{18}]^-$, Kauffman et al. achieved 100% Faradaic efficiency (FE) for CO, although the rates were low even at higher potentials.^[57] Alkynyl-protected $[\text{Ag}_{15}(\text{C}\equiv\text{C}-t\text{Bu})_{12}]$ was shown to demonstrate $\text{FE}_{\text{CO}(\text{max})}$ of 95.0% at -0.6 V.^[58] Kim et al. compared the relative performance of the thiolate-protected Ag/Au-MNCs comprising $[\text{Au}_{25}(\text{SR})_{18}]$, $[\text{Ag}_{25}(\text{SR})_{18}]$, and $[\text{AuAg}_{12}@\text{Au}_{12}(\text{SR})_{18}]$ NCs, which exhibited an industrially relevant current density of 200 mA cm^{-2} .^[59] Various factors such as ligand effects,^[60] size and morphology of clusters,^[61] doping and alloying,^[62,63] and polymerization^[64] have been studied to probe their influence on $e\text{CO}_2\text{R}$ activity. Nuclearity of MNCs is a unique modulation tool in this regard, not only

because of the conventional surface area effect, but also, the resultant surface charge tunability of the active metal sites on the outer motifs and the ligament. Very few studies have critically examined this aspect while also controlling the performance of NCs for CO production. Seong et al., conducted an activity comparison on Au_{25} , Au_{38} , and Au_{144} model catalysts, although their study primarily focused on the identification of active sites after de-thiolation, where contrary to the conventional trend, the activity order was found to increase with the size.^[65] Li et al. studied the comparative activity of Au NCs with different sizes (1–2.5 nm regime) to find out a higher surface-to-volume ratio in smaller size NCs leads to a higher $e\text{CO}_2\text{R}$ -CO activity.^[66] Zhou et al. mapped out three distinct size-dependent states (metallic [>2.3 nm], transition regime [2.3–1.7 nm], and non-metallic or excitonic states [<1.7 nm]) for thiolate-protected Au_{25} , Au_{38} , Au_{144} , Au_{333} , $\text{Au}_{\approx 520}$ and $\text{Au}_{\approx 940}$ clusters and showed its impact on electrocatalytic CO and alcohol oxidation.^[67] Despite these studies, a clear gap exist in the elucidation of lucid structure-activity rationales on the influence of the nuclearity of Ag-NCs and the ligands on $e\text{CO}_2\text{R}$ -to-CO performance outcomes.

To bridge that, herein, we report the comparative electrocatalytic efficiency of three atomically precise silver nanoclusters, i.e., $[\text{Ag}_{21}(\text{MCT})_{12}(\text{TPP})_2]^+$, $[\text{Ag}_{31}(\text{TRZ})_{10}]^{2-}$ and $[\text{Ag}_{42}(\text{CBDT})_{15}(\text{TPP})_4]^{2-}$ (abbreviated as Ag_{21} , Ag_{31} , and Ag_{42} , respectively), demonstrating highly selective $e\text{CO}_2\text{R}$ -to-CO activity at competitive rates under low overpotentials.^[68–70] The Ag_{21} and Ag_{42} clusters are bound by carborane-thiolate cages, viz. *meta*-carborane-9-thiol (MCT-H), and *ortho*-carborane-1,2-dithiol (CBDT- H_2), respectively. The Ag_{31} cluster comprises TRZ ligand shell (where TRZ- H_2 is 6-(dibutylamino)-1,3,5-triazine-2,4-dithiol). The study also attempts at elucidating the relative influence of nuclearity and ligand modulation on the catalytic behaviour of Ag NCs for $e\text{CO}_2\text{R}$. To that end, we explored two reported nanoclusters, $[\text{Ag}_{22}(\text{dppe})_4(2,5\text{-DMBT})_{12}\text{Cl}_4]^{2+}$ (abbreviated as Ag_{22}) and $(\text{PPh}_4)_4[\text{Ag}_{44}(\text{SPhF}_2)_{30}]$ (abbreviated as Ag_{44}), to carry out control experiments with NCs having comparable nuclearity (Ag_{21} & Ag_{22} NC and Ag_{42} & Ag_{44} NC) but different ligands (carborane-thiol and benzene-thiol).^[71,72] Ligands can modulate the electronic density of the metal core through inductive and delocalization effects and also impact the structural properties, accessibility of active sites, and surface hydrophobicity. Consequently, nanoclusters with comparable nuclearity can display similar baseline activity, although their selectivity and efficiency may vary depending on the nature of the protecting ligands.

Ag_{21} NC achieved a near-unity $\text{FE}_{\text{CO}(\text{max})}$ of 99.6% at a low potential of -0.59 V vs RHE and a maximum partial current density for CO ($j_{\text{CO}(\text{max})}$) of 148 mA cm^{-2} at -0.7 V vs RHE. In contrast, the larger Ag_{31} and Ag_{42} NCs exhibited slightly lower $\text{FE}_{\text{CO}(\text{max})}$ of 97% and 95%, respectively. Interestingly, the potentials for $\text{FE}_{\text{CO}(\text{max})}$ and $j_{\text{CO}(\text{max})}$ were observed to shift by ≈ 70 and ≈ 80 mV respectively for every ≈ 10 Ag atoms in the NC. Several spectroscopic techniques were explored to probe the relative electronic and chemical properties of the Ag NCs. Quantum chemical studies simulated the adsorption of intermediates $^*\text{COOH}$ and $^*\text{CO}$ at different catalytic sites of Ag_{21} and Ag_{42} corroborating the better performance of Ag_{21} from the thermodynamic standpoint. The enhanced overlap between the Ag (5d) and C (2p) states and increased charge delocalization are primarily responsible for

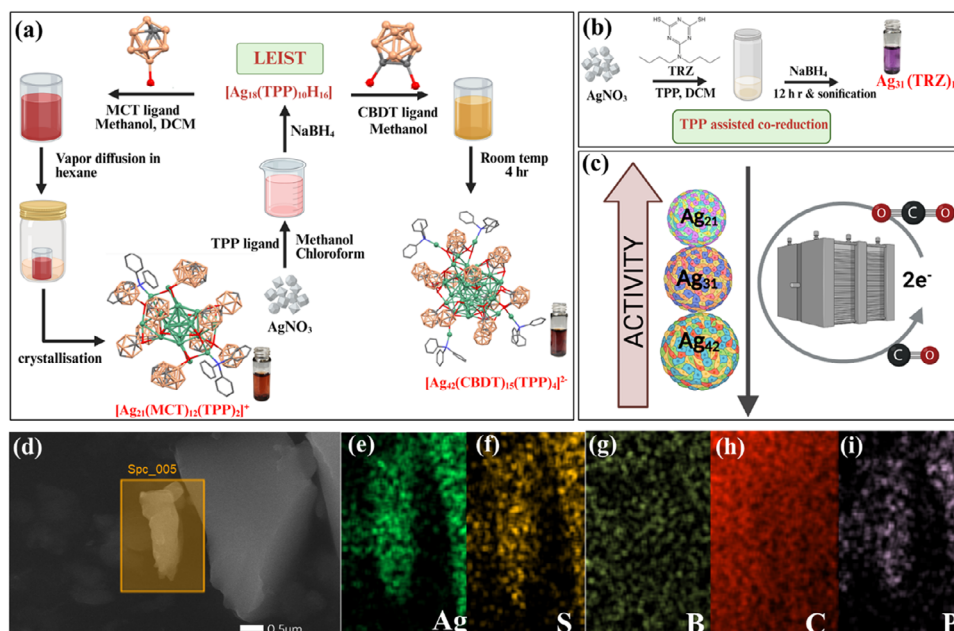


Figure 1. Schematic illustration of the synthesis of $[\text{Ag}_{21}(\text{MCT})_{12}(\text{TPP})_2]^+$ and $[\text{Ag}_{42}(\text{CBDT})_{15}(\text{TPP})_4]^{2-}$ using LEIST reaction starting from Ag_{18} NC. b) Synthesis Scheme of the TPP-assisted co-reduction method for synthesizing $[\text{Ag}_{31}(\text{TRZ})_{10}]^{2-}$ cluster. c) Schematic of the relative performance of three Ag NCs for eCO_2R . d) SEM image of microcrystalline Ag_{21} NC before loading on the GDE (Scale Bar is 0.5 μm). e–i) EDS elemental mapping of the selected region showing the presence of Ag, S, B, C, and P elements.

the activity enhancement on Ag_{21} . This would allow for greater charge transfer from Ag to the C atoms of $^*\text{COOH}$, leading to stronger intermediate binding and a lower overpotential on Ag_{21} .

2. Results and Discussion

2.1. Synthesis and Characterization of Ag Nanoclusters

Three distinct Ag NCs, with varying nuclearity of the Ag core (about ten Ag atoms each), are chosen for examination of their eCO_2R performance. The thermal and ambient stable Ag NCs, Ag_{21} , Ag_{31} , and Ag_{42} were synthesized according to our earlier report.^[68–70] $[\text{Ag}_{21}(\text{MCT})_{12}(\text{TPP})_2]^+$, and $[\text{Ag}_{42}(\text{CBDT})_{15}(\text{TPP})_4]^{2-}$ are coprotected by carborane-thiolate (MCT or CBDT) and TPP ligands, which are synthesized from TPP and hydride-protected $[\text{Ag}_{18}(\text{TPP})_{10}\text{H}_{16}]^{2-}$ cluster, using ligand exchange-induced size or structure transformation (LEIST) method (where TPP is triphenylphosphine) (Figure 1a). Nanoclusters having carborane (featuring an icosahedral C_2B_{10} cage) or TRZ-based ligands, rarely explored for catalytic applications so far, are expected to impart remarkable chemical resistance and unique electronic properties boosting eCO_2R performance.^[73,74]

$[\text{Ag}_{31}(\text{TRZ})_{10}]^{2-}$ cluster was synthesized through a single-step, TPP-assisted co-reduction reaction of silver, TRZ-dithiolate, and TPP precursors using sodium borohydride as a reducing agent (Figure 1b). TRZ is a six-membered aromatic heterocycle with three nitrogen atoms at positions 1, 3, and 5. The hexagonal triazine ring is less electron-dense than benzene due to the electron-withdrawing capacity of the three nitrogens. A detailed synthesis procedure of the Ag NCs can be found in the experimental section. The gas diffusion electrodes (GDE) were prepared via spray coating of the purified Ag NC powders, to carry out eCO_2R in a

flow cell setup. Figure 1c illustrates the effect of the decreasing nuclearity/size of Ag NCs on the catalytic activity. Field-emission scanning electron microscopy (FE-SEM) of Ag_{21} , before electrode loading, displayed microcrystallites having nanoplatelet-like morphology (Figure 1d). Elemental mapping via energy dispersive spectroscopy (EDS) showed the presence of Ag in addition to S, B, C, and P elements with nominal stoichiometry (Figure 1e–i). The mass and atomic percentage of each element are shown in the EDS spectra in Figure S1 (Supporting Information).

Molecular characterization of the clusters were conducted through UV–vis absorption spectroscopy and high-resolution mass spectrometric studies. UV–vis spectrum exhibited multiple absorption bands for the NCs associated with the size confinement and discrete electronic energy levels. Four characteristic peaks were observed for the Ag_{21} in DCM solution at 305, 355, 396, and 494 nm, along with a broad peak at 697 nm (Figure 2a). Ag_{31} NC exhibits absorption peaks at 402, 525, and 593 nm, respectively, and the Ag_{42} cluster shows two absorption peaks at 571 and 456 nm (Figure 2b,c). Photographic images of all three cluster solution are shown in Figure S2 (Supporting Information). The specific absorption peak patterns from UV–Vis spectra match well with our earlier reports confirming the chemical purity of the clusters (Figure S3, Supporting Information).^[68–72] Time-dependent UV–vis measurements showed stability of these clusters up to 2 months at ambient conditions. The molecular compositions of Ag NCs in solution were investigated using high-resolution electrospray ionization mass spectrometry (ESI-MS). The ESI-MS of the Ag_{21} cluster in positive-ion mode show a prominent peak at m/z 4893.24 in mono positive charge state. The molecular composition of the cluster is assigned as $[\text{Ag}_{21}(\text{MCT})_{12}(\text{TPP})_2]^+$, and the isotopic distribution of the experimental peak matches the simulated pattern well. Two additional

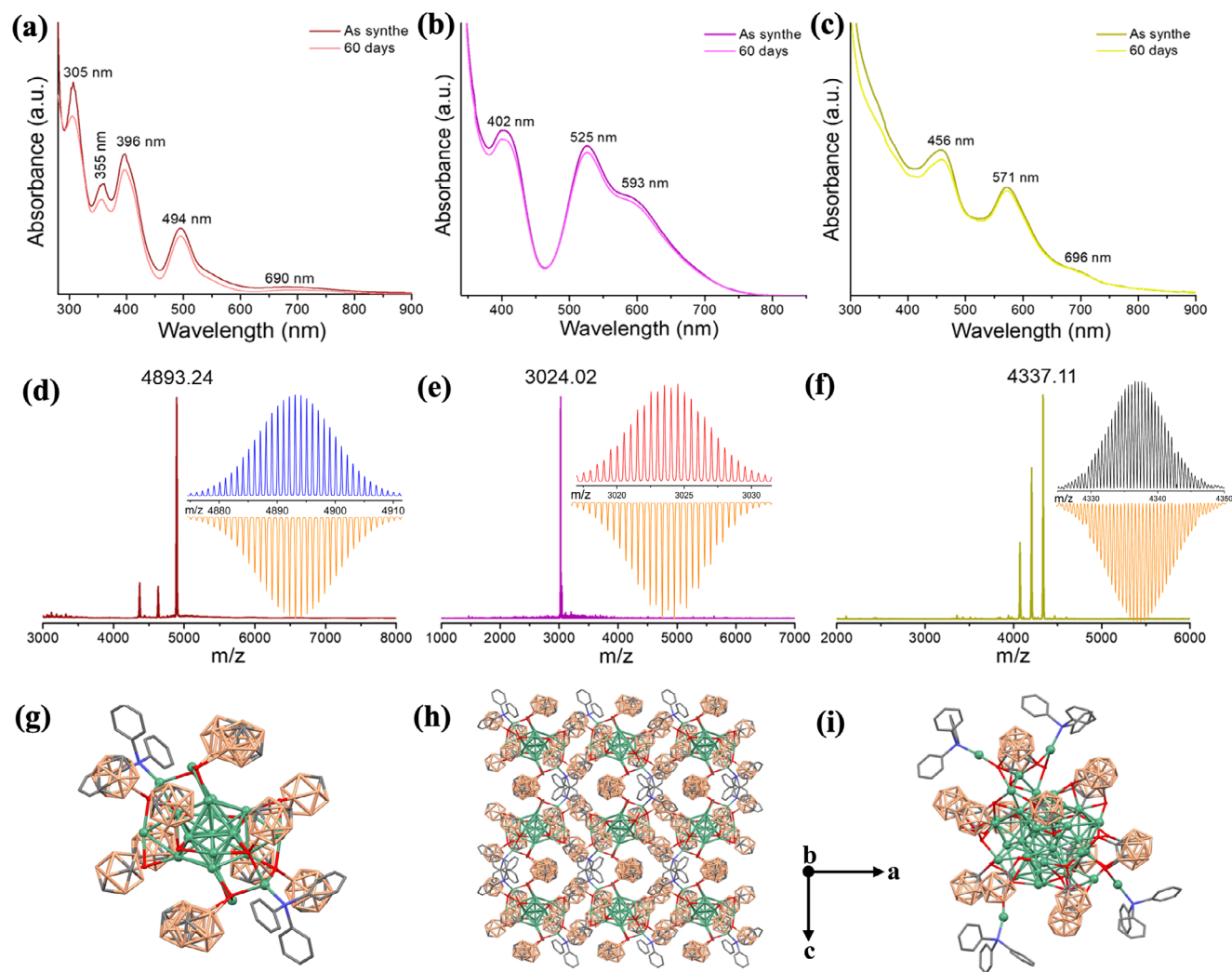


Figure 2. Characterization of Ag NCs. UV–vis absorption spectra of a) Ag_{21} , b) Ag_{31} , and c) Ag_{42} clusters before loading on the GDE, showing long-term stability at ambient condition, d–f) High-resolution mass spectrometric data of the catalyst materials, with inset showing the comparison of respective experimental and simulated spectra, g) single crystal molecular structure of Ag_{21} NC, h) Fully packed structure of Ag_{21} NC, i) DFT optimized structure of Ag_{42} . All the structures are along the direction of the b axis. Color legend - dark green: silver, red: sulfur, blue: phosphorus, light orange: boron. gray: carbon. The SCXRD structural data of Ag_{21} and the DFT optimized structure of Ag_{42} have been used from reported literature.^[68,70]

minor peaks at m/z 4630.5 and m/z 4368.35 indicate sequential losses of TPP from the parent cluster (Figure 2d). The ESI-mass spectrum of the Ag_{31} in negative-ion mode indicates a prominent peak at m/z 3024.02 (Figure 2e). A peak-to-peak spacing of 0.5 for m/z 3024.02 confirms the presence of the dianionic state. In the case of the Ag_{42} nanocluster, a prominent peak was observed at m/z 4337.11, with an isotopic peak-to-peak separation of 0.5, indicative of a dianionic charge state. Additionally, two less intense peaks appear at m/z values of 4205.67 and 4074.21, which corresponded to the removal of TPP ligands from the parent cluster (Figure 2f). The Ag_{22} NC exhibit a peak at m/z 2877.39 having 2^+ charge state, in good agreement with the simulated spectra, as shown in Figure S4 (Supporting Information). Negative ion mode ESI-MS of Ag_{44} exhibits a prominent peak at m/z 2853.29 corresponding to the 3^- charge state, along with a minor peak at 2140.20 corresponding to the 4^- charge state of Ag_{44} cluster. Single-crystal structure of Ag_{21} NC showed that it has a central

icosahedral Ag_{13} core and a shell of eight silver atoms, while the DFT-optimized structure of Ag_{42} has a larger Ag_{28} core and a shell of 14 silver atoms (Figure 2g–i; Figure S5, Supporting Information). Thiolates are bound to the cluster through Ag–S bonds, while Ag–P linkages coordinate with phosphines.

Transmission electron microscopy (TEM) analysis shows the nanosized structures of Ag_{21} , Ag_{31} , and Ag_{42} , with particle sizes ranging from 1.5 to 3 nm (Figure 3a–c and Figure S6 (Supporting Information)). The overall size of the NC (including the ligand) falls well within the NC size regime. The presence of Ag and other elements in Ag_{21} NC can be observed in Figure S7 (Supporting Information), showing the elemental mapping in HAADF-STEM (High-Angle Annular Dark Field Scanning Transmission Electron Microscopy). The IR spectra of Ag_{21} and the free MCT ligand were measured and compared (Figure 3d). The presence of carborane was confirmed from the appearance of C–B and B–B vibrational peaks at 1050 and 866 cm^{-1} , respectively.

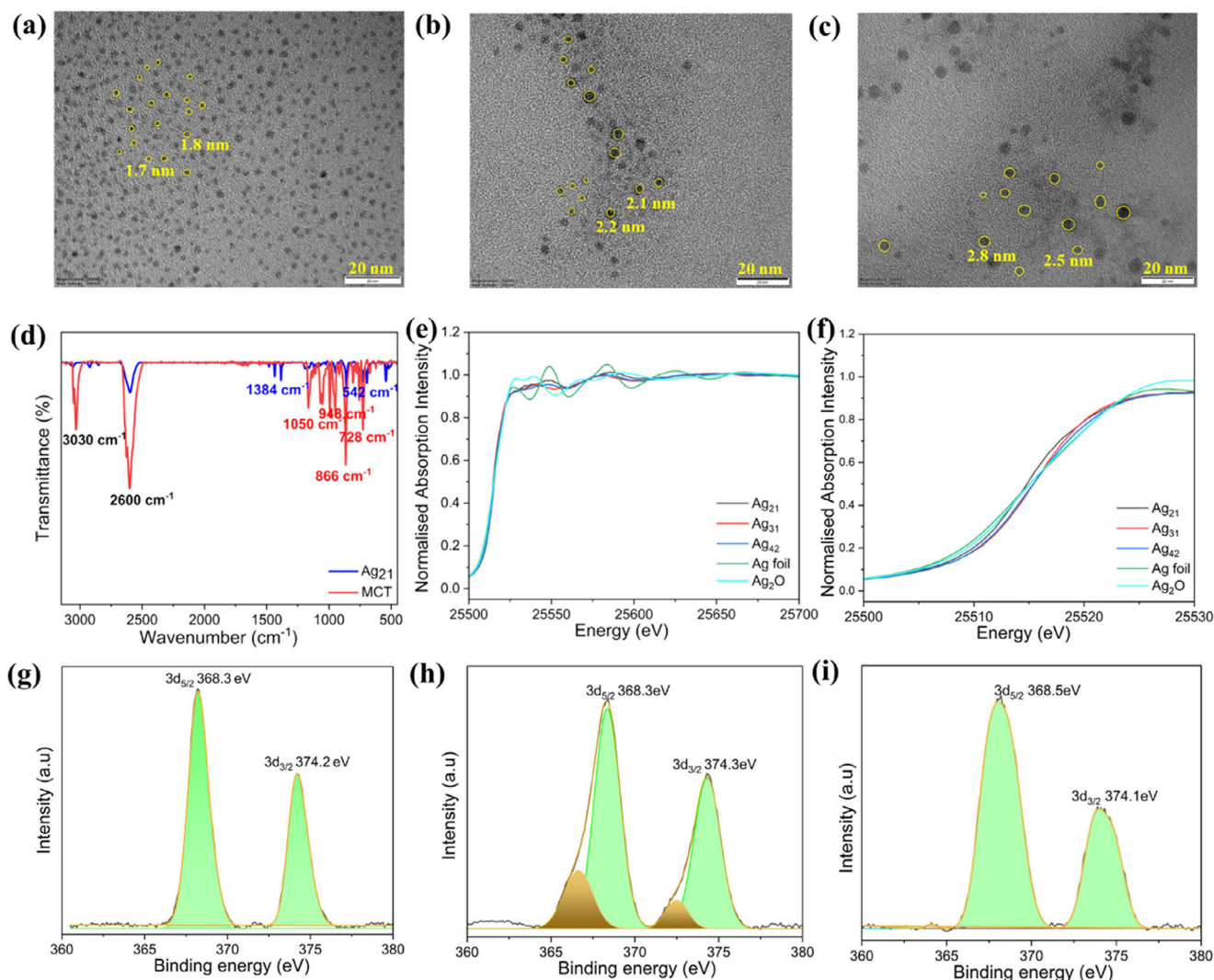


Figure 3. TEM images showing ultrasmall particle distribution for the clusters of a) Ag₂₁ b) Ag₃₁ c) Ag₄₂. d) Full range FTIR spectra of Ag₂₁ NC and MCT ligand, e,f) XANES spectra of Ag₂₁, Ag₃₁ and Ag₄₂ catalysts with reference samples (Ag foil and Ag₂O) at Ag-K edge indicating intermediate oxidation states, g–i) selected area HR-XPS spectra of Ag 3d region of Ag₂₁, Ag₃₁, Ag₄₂, respectively.

Another band observed at 1384 cm⁻¹ corresponds to the stretching frequency of the N–O bond of NO₃⁻ counterions. Likewise, measurements and comparisons of the FT-IR spectra of Ag₄₂ and free CBDT ligands are shown in Figure S8b (Supporting Information). For Ag₃₁, peaks at 743 and 1543 cm⁻¹ are consistent with C–S stretching from the thiol and the C=N stretching, respectively, which are constituents of the TRZ ligand (Figure S8a, Supporting Information). The electronic states analyzed through X-ray Absorption Near Edge Structure (XANES) (Figure 3e–f) suggest mixed oxidation state of the Ag atoms in the Ag NCs. This can be attributed to the different charge distribution on the Ag atoms arising from their distinct chemical environments at the core and surface of the clusters. This is further supported by the Bader charge analysis conducted through theoretical calculations (Tables S4 and S5, Supporting Information).

Further XPS analysis was conducted on Ag NCs to investigate the elemental and chemical composition of the clusters. All the clusters exhibited peaks corresponding to Ag 3d_{5/2} and Ag

3d_{3/2}. Ag₂₁ showed an Ag 3d_{5/2} peak at 368.2 eV and Ag 3d_{3/2} peak at 374.3 eV, indicating the presence of mostly metallic silver (Ag (0)) (Figure 3g). In addition to Ag, XPS also revealed the elements present in the MCT and TPP ligand. The intense peaks observed in the XPS survey spectra of Ag₂₁ NC at 189.7 and 284.8 eV, confirmed the presence of B and C (Figure S9a, Supporting Information), respectively, in the carborane ring. The deconvoluted C 1s and B 1s are shown in Figure S9b,c (Supporting Information). The sulfur in carborane thiolate shows peaks at 164.2 eV for S 2p_{3/2} and 162.4 eV for S 2p_{1/2} (Figure S9d, Supporting Information). Similarly, P 2p spectra show peaks at 129.3 and 130.2 eV, corresponding to the P 2p_{1/2} and P 2p_{3/2}, respectively, corresponding to the phosphorus in the TPP ligand (Figure S9e, Supporting Information). For Ag₃₁ NC, apart from Ag (Figure 3h), N 1s and S 2p were observed in the XPS survey scan at peak positions of 399.5 and 164.5 eV, arising from the TRZ ligand (Figure S10a, Supporting Information). From the C1s spectra, the peak due to the C=N bond in TRZ is visible at

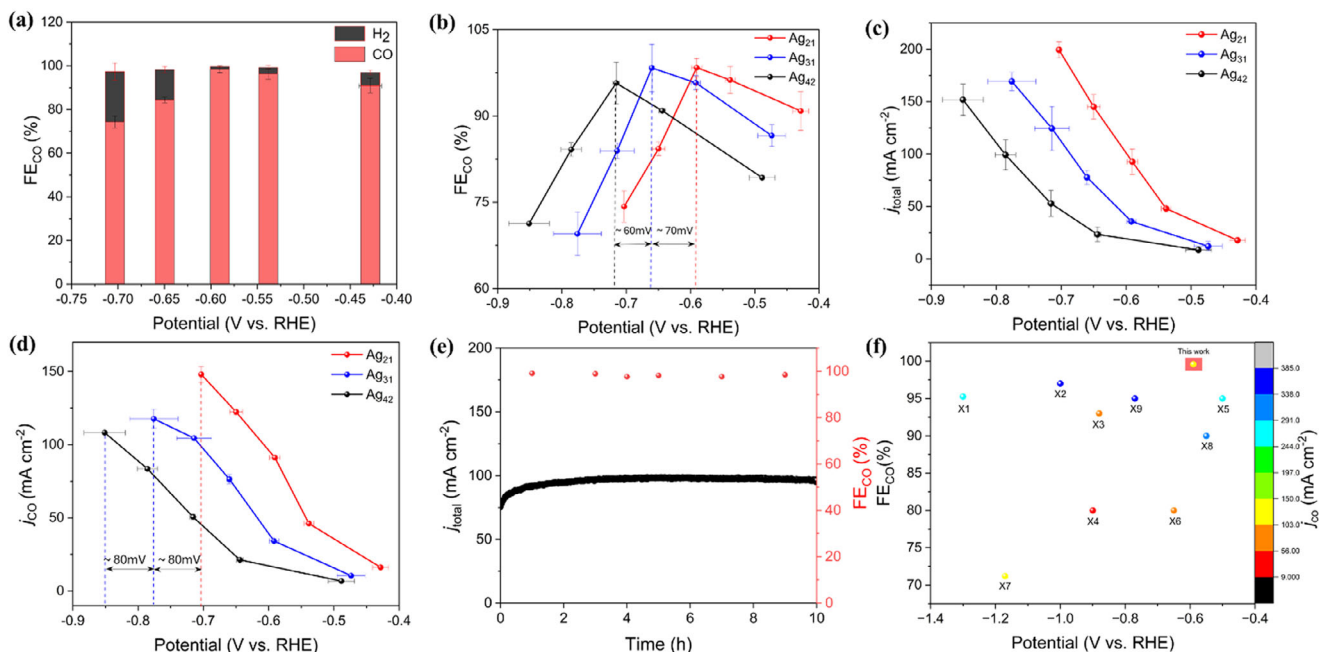


Figure 4. eCO₂R performance of Ag NCs in 1 M KOH in an alkaline flow cell. a) FE (%) of products with varying potential for Ag₂₁, b) FE (%) of CO with varying potential for all the clusters c) total current density across the potential range for Ag₂₁ the three Ag NCs, d) partial current density for CO (j_{CO}) across the potential range for all the clusters, e) Electrochemical stability plot of Ag₂₁ measured at a constant voltage of -0.59 V vs RHE, f) FE_{CO} vs potential plots illustrating comparison between various reported Ag-based catalysts (primarily nanoclusters) and Ag₂₁ for eCO₂R-to-CO, in flow cell systems. The entries for the plot has been provided in Table S2 (Supporting Information).

peak position 286.5 eV (Figure S10b, Supporting Information). The peaks at 399.6 and 401.2 eV in the N1s spectra, correspond to C–N and C=N bonds in TRZ ligands (Figure S10c, Supporting Information). Similarly, the XPS spectra of Ag₄₂ NC, showed the presence of Ag (Figure 3i) and other elements present in the ligands (Figure S11, Supporting Information).

2.2. Electrochemical Performance of Ag Nanoclusters

The electrocatalytic CO₂ reduction performance of the Ag clusters (Ag₂₁, Ag₃₁, and Ag₄₂) was evaluated in a flow cell with a 1 M KOH electrolyte in the potential range of -0.4 to -0.9 V vs RHE. For all three nanoclusters, CO is the primary product generated upon electrochemical CO₂ reduction, with H₂ as a minor byproduct. With minimal HER side reaction, the FE_{CO(max)} for Ag₂₁-loaded GDE turned out to be 99.6% at -0.59 V (vs RHE) (Figure 4a). As the nuclearity of the clusters increased, the FE_{CO(max)} gradually declined; the highest nuclearity cluster, Ag₄₂, exhibited the lowest FE_{CO(max)}, 95%, at a more negative potential of -0.71 V vs RHE, and the Ag₃₁ NC-loaded GDE achieved FE_{CO(max)} 97% at ≈ -0.67 V vs RHE (Figure 4b; Figure S12, Supporting Information). To understand the relative effect of nuclearity and ligand contributions on the eCO₂R performance, we further examined Ag₂₁ and Ag₂₂ nanoclusters, which possess nearly identical nuclearity but are stabilized by different ligands. Ag₂₂ exhibited a FE_{CO(max)} of 96.2% at -0.6 V ($j_{\text{CO}} = 78$ mA cm⁻²), which is slightly lower than that of Ag₂₁ under similar conditions (Figure S13a,b, Supporting Information). The comparable nuclearity of these two clusters minimizes size-dependent influ-

ences, thereby allowing a direct assessment of ligand and associated effects. The slightly higher performance of Ag₂₁ (FE_{CO(max)} is 99.6% at -0.59 V vs RHE, j_{CO} is 91 mA cm⁻²) is attributed to the carborane-thiol ligands, which impart both electronic modulation through charge delocalization and redistribution of surface electron density, as well as may have other structural and physico-chemical effects such as reduced steric hindrance, enhanced site accessibility, and different surface hydrophobicity. Together, these factors can promote more efficient CO₂ activity compared to the benzene-thiol-protected Ag₂₂. However, broadly speaking, the nuclearity of the clusters was found to have a more dominant effect on the overall performance of the clusters. Extending this analysis to higher nuclearity systems, Ag₄₄ achieved a FE_{CO(max)} of 90.2% at -0.74 V, which is lower than that of Ag₄₂ at -0.71 V (FE_{CO(max)} of 95%) (Figure S14a,b, Supporting Information). This trend again highlights the superior performance of carborane-based (CBDT) ligands relative to benzenethiol-based (SPhF) ligands in steering CO₂ electroreduction, underscoring the influence of ligand-modulated structural and electronic effects in dictating nanocluster reactivity. Interestingly, we note that while the value of FE_{CO(max)} varies, the potential for FE_{CO(max)} matches closely for clusters with similar nuclearity (Ag₂₁/Ag₂₂ and Ag₄₂/Ag₄₄).

The total current density also followed the similar trend of FE_{CO(max)}, with Ag₂₁ reaching 200 mA cm⁻² at -0.7 V vs RHE, outperforming Ag₃₁ and Ag₄₂ which reached 169.2 and 151 mA cm⁻² at more negative potentials of -0.77 V vs RHE and -0.85 V vs RHE, respectively (Figure 4c). The Ag₂₁-loaded GDE exhibited the highest partial current densities for CO (j_{CO}), reaching 148 mA cm⁻² at -0.7 V vs RHE, whereas Ag₃₁ and Ag₄₂ exhibited

117 mA cm⁻¹ at -0.77 V vs RHE and 108 mA cm⁻¹ at -0.85 V vs RHE (Figure 4d). Comparative studies show that Ag₂₂ exhibits a $j_{\text{CO(max)}}$ of 130 mA cm⁻² and a j_{max} (maximum total current density) of 187 mA cm⁻² at -0.71 V, respectively (Figure S13c,d, Supporting Information), which are slightly lower than those of Ag₂₁. Similarly, Ag₄₄ delivered a lower activity than Ag₄₂ with a $j_{\text{CO(max)}}$ of 82.75 mA cm⁻² and a j_{max} of 141.65 mA cm⁻² at a higher potential of -0.88 V (Figure S14c,d, Supporting Information).

The electrocatalytic stability of Ag₂₁ was investigated in a flow cell at -0.59 V vs RHE. For up to 10 h, the CO selectivity remained steady at about FE_{CO} of 99% (Figure 4e). We also extended the stability test at the same potential for over 50 h and observed that both the total current density (j_{total}) and FE_{CO} remained largely stable (Figure S15, Supporting Information). However, the performance was occasionally disturbed by systemic issues such as flooding of the gas diffusion layer (GDL) due to salt deposition, which hinder CO₂ transport, diminishing the activity. This issue was mitigated through periodic washing of the GDL with water. The Ag₂₁ exhibited a TOF of 0.36 s⁻¹ at the potential -0.7 V vs RHE, where j_{CO} was found to be maximum. Further, to assess the catalyst stability, structural and chemical integrity were examined through XPS analysis (Figures S16–S18, Supporting Information). Pre- and post-electroreduction XPS spectra revealed that Ag₂₁ and Ag₃₁ retained their chemical and electronic states, indicating robust cluster stability. The presence of minor satellite peaks in the Ag 3d XPS spectra after electrocatalysis may arise from negligible Ag-O formation due to adsorbed KOH electrolyte on the surface. EXAFS (Extended X-ray Absorption Fine Structure) analysis (Figures S19 and S20 and Table S1, Supporting Information) confirmed the presence of Ag–S bonds in both Ag₂₁ and Ag₄₂ after the reaction, further supporting the structural integrity and stability of these nanoclusters during CO₂ electroreduction.

2.3. Mechanistic Understanding of eCO₂R Activity from DFT Studies

Density functional theory (DFT) was employed to study the CO₂ to *CO mechanism over Ag₂₁ and Ag₄₂ clusters using the Vienna ab initio simulation package (VASP)^[75] with the Perdew–Burke–Ernzerhof (PBE)^[76] functional under generalized gradient approximation (GGA).^[77] *Computational Details in Supporting Information* provide the detailed information. To circumvent the computational cost, a single molecular unit of Ag₂₁ and Ag₄₂ was modelled and considered for further calculations. The DFT-optimized geometries, in terms of their metal and ligand arrangement, are shown in Figure 5a,b, respectively. The negative E_{int} (interaction energy) of Ag₂₁ and Ag₄₂ complexes represent the thermodynamic stability of these clusters under the electrocatalytic condition of eCO₂R due to stabilization effect of the carborane-thiol ligands (Table S3, Supporting Information). Interestingly, Bader charge analysis reveals distinct charge distributions across different regions of the Ag clusters, suggesting varying oxidation states of Ag atoms in the staple motifs and core regions, as tabulated in Tables S4 and S5 (Supporting Information). To compare their activity, adsorption of *COOH and *CO (asterisk symbol (*) denotes the adsorbed species) was simulated at different heterogeneous sites, as represented in Figures

S21 and S22 (Supporting Information), and the most stable optimized configurations were selected for further analysis. The higher number of local minima in Ag₂₁ clusters indicates greater surface accessibility for intermediate binding, in contrast to the sterically hindered Ag₄₂ clusters with limited exposed active sites. In the most stable geometries, the *COOH and intermediates preferentially bind to the one-fold top positions of Ag atoms that are bridged between two S atoms, indicating that the exposed Ag atoms on the surface act as the active sites for the eCO₂R activity in these clusters. Notably, the carbon atoms of these intermediates on Ag₂₁ clusters exhibit a higher charge density (i.e., are less positively charged) compared to those on Ag₄₂ clusters (Figure S23, Supporting Information). This increased electron density likely enhances the activation of the initial intermediates, accounting for the higher catalytic activity of Ag₂₁ clusters.

Using the computational hydrogen electrode (CHE) model,^[78] we calculated the thermodynamic Gibbs free energy (ΔG) associated with the CO₂ to *CO formation, following the adsorbate-evolution mechanism (AEM) via a concerted proton-electron transfer (CPET) pathway (Figure 5c). The lower ΔG values of 0.42 eV observed for Ag₂₁, in comparison to 1.21 eV for Ag₄₂, suggest that the smaller Ag₂₁ clusters exhibit superior catalytic activity for eCO₂R, which can be attributed to its size-dependent surface charge density and electronic structure. Due to their smaller size, the Ag₂₁ cluster exhibits a large number of undercoordinated surface atoms, leading to greater charge localization and a more negatively charged surface (Figure 5d). This increased surface charge facilitates stronger electrostatic interactions with the CO₂ molecule, stabilizing the adsorption and subsequent activation of the molecule during the CPET step. To further examine the effect of cluster size and ligand environment on catalytic performance, we compared the eCO₂R activity of Ag₂₁, Ag₄₂, and Ag₄₄ clusters, where Ag₄₄ was studied with different ligands, and heterogeneous sites were investigated for stable adsorption positions (Figure S24, Supporting Information). The higher ΔG value of Ag₄₄ (1.29 eV), relative to Ag₂₁ (0.42 eV) and Ag₄₂ (1.21 eV) indicates its lower eCO₂R activity (Figure S25, Supporting Information).

The electronic structure analysis reveals that in Ag₂₁, there is an enhanced orbital overlap between Ag (5d) and C (2p) states within the -2 to -4 eV range (Figure 5e; Figure S26, Supporting Information). This stronger orbital interaction facilitates more efficient charge transfer from the Ag surface to the adsorbed *COOH intermediate, thereby enhancing its stabilization and lowering the energy barrier for its formation. In contrast, the larger Ag₄₂ clusters, with more bulk-like features and lower surface charge density per active site, exhibit weaker site CO₂ interactions and less efficient charge transfer, leading to higher ΔG values. In addition to the orbital overlap between Ag (5d) and C (2p) orbitals, we observed a strong overlap between the frontier orbitals of Ag (5d) and S (3p) orbitals, highlighting their strong interactions in Ag₂₁ and Ag₄₂ clusters, as represented in Figures S27 and S28 (Supporting Information). Such strong interaction between Ag and P atoms contributes to the enhanced stability of these clusters under eCO₂R conditions. Thus, the superior CO₂ reduction activity of Ag₂₁ is intrinsically linked to the synergistic effects of cluster size, surface charge accumulation, and site-specific electronic interactions, together modulating the reaction

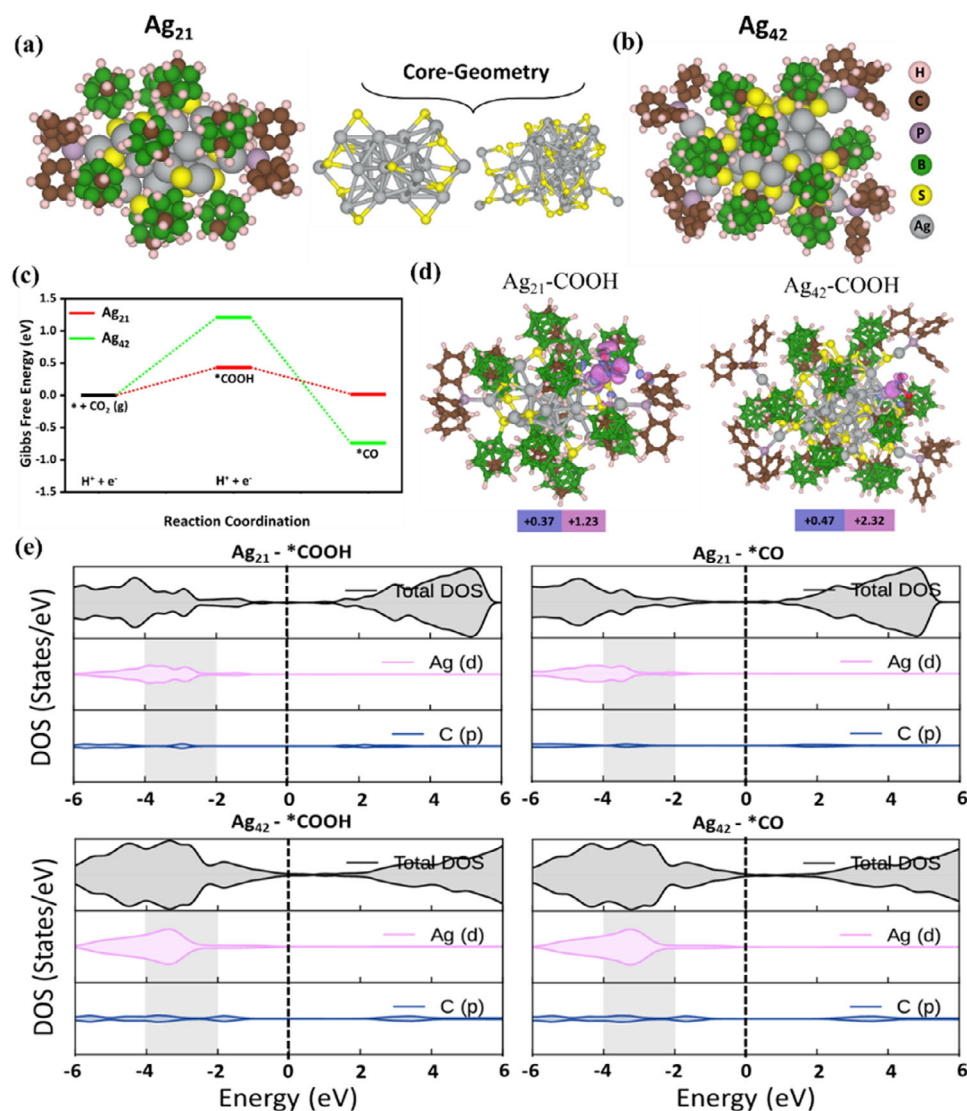


Figure 5. Optimized geometries of a) Ag_{21} and b) Ag_{42} clusters, with multiple heterogeneous active sites for intermediate adsorption represented in Figures S22 and S23 (Supporting Information). c) Gibbs free energy diagram of Ag_{21} and Ag_{42} clusters, with the black solid horizontal line denoting the neutral surface reference. d) Charge density difference (CDD) plots at an isosurface of $0.002 \text{ eV \AA}^{-3}$, where pink and green regions indicate charge accumulation and depletion, respectively. Numeric values represent charge transfer (in $|e|$ units) derived from Bader charge analysis on Ag and C atoms. e) Subplots for total and partial density of states (DOS) for Ag (5d) and C (2p) states, with the Fermi-level set at 0.00 eV. Note that total and partial DOS analysis for pristine, $\ast\text{COOH}$, and $\ast\text{CO}$ -adsorbed Ag_{21} and Ag_{42} clusters are provided in Figure S25 (Supporting Information).

energy profile by enhancing the stabilization of key reaction intermediates.

3. Conclusion

To summarize, this study provides an account of the comparative eCO_2R -to-CO activity of three Ag nanoclusters with varying nuclearity of \approx ten Ag atoms between them. The order of activity and $\text{FE}_{\text{CO}(\text{max})}$ (selectivity) is found to follow the trend of decreasing metal cluster atomicity/size. Ag_{21} , being the smallest nanocluster, demonstrates excellent performance in electrochemical reduction of CO_2 to CO, achieving a near-unity $\text{FE}_{\text{CO}(\text{max})}$ of 99.6% at a low applied potential of -0.59 V vs RHE, indicating exceptional selectivity with minimal parasitic reactions. The j_{max}

of 200 mA cm^{-2} underscores its ability to drive CO_2 conversion at high rates. Interestingly, an increase of ten Ag atoms across the clusters was found to shift the $\text{FE}_{\text{CO}(\text{max})}$ and $j_{\text{CO}(\text{max})}$ potentials (for CO production) by 70 and 80 mV, respectively, showcasing a semi-quantitative correlation. The enhanced activity can be attributed to the distinct structural and electronic features of the Ag_{21} cluster. Its small size ensures a high surface-to-volume ratio and a relatively larger fraction of low-coordination Ag atoms, both of which contribute to an increased density of active sites. Moreover, the Ag_{21} cluster displays favorable electronic interactions that facilitate the CO_2 reduction reaction. Specifically, the overlap between the Ag 5d orbitals and the C 2p orbitals of CO_2 and key reaction intermediates, such as $\ast\text{COOH}$ and $\ast\text{CO}$, leads to enhanced adsorption and activation of reactant molecules and

intermediates. The delocalization of electronic charge across the cluster further supports efficient electron transfer and stabilizes the reaction intermediates, thereby lowering the activation energy barrier and improving the overall reaction kinetics. Together, these factors establish Ag₂₁ as an efficient catalyst for CO₂ electroreduction, with its performance closely tied to its unique atomic configuration and frontier orbital characteristics. Interestingly, control experiments in this case, reveal a more dominant effect of nuclearity in dictating the baseline activity of Ag nanoclusters, while ligands impart subtle yet significant contributions that fine-tune selectivity and activity. Such enhancements, arising from electronic modulation and structural accessibility provided by the ligand shell, underscore the importance of ligand engineering in steering eCO₂R performance beyond nuclearity alone. Fundamentally, this study attempts to elucidate some new structure-activity insights in metal nanocluster-driven CO₂ electroreduction that can find broader applications in establishing materials design rationales in this field.

4. Experimental Section

Chemicals Used: Silver nitrate was bought from Rankem Chemicals. Triphenylphosphine, 2,5-dimethylbenzenethiol, 3,4-difluorobenzenethiol, tetraphenylphosphonium chloride, tetraphenylphosphonium bromide, 1,2-bis(diphenylphosphino)ethane, and sodium borohydride (98%) were purchased from Aldrich and Sigma-Aldrich Chemicals. The *meta*-carborane 9-thiol and *ortho*-carborane-1,2-dithiol were synthesized using carborane derivatives, bought from Katchem s.r.o. (Czech Republic). The TRZ-H₂ ligand was acquired from TCI America. Chloroform (CHCl₃), *n*-hexane, *N,N*-dimethylformamide (DMF), solvent grade dichloromethane (DCM), trimethylamine, and methanol (99.5%) were acquired from Rankem Chemicals and Finar, India. All the chemicals were commercially available and used as such without any further purification.

Synthesis of Ag₂₁ and Ag₄₂ Nanoclusters: The Ag₂₁ and Ag₄₂ clusters were synthesized through a LEIST reaction starting from the [Ag₁₈(TPP)₁₀H₁₆] cluster, following the earlier reports.^[68,70] The precursor [Ag₁₈(TPP)₁₀H₁₆] was synthesized through a single-step reduction of AgNO₃ (20 mg) and TPP (70–75 mg) mixture in methanol-chloroform (1:2 v/v) solution, under constant stirring at room temperature. Later, sodium borohydride (6.5 mg) solution dissolved in 1 mL of Milli-Q water was added to the prior mixture. After 3–3.5 h, the reduction reaction results in the dark green solution, which indicates the formation of the desired nanocluster.

The Ag₂₁ was synthesized via LEIST reaction between [Ag₁₈(TPP)₁₀H₁₆] and MCT-H. ≈10 mg of the Ag₁₈ precursor nanocluster was dissolved in 5 mL of methanol and mixed with 8 mg of MCT-H. The solution gradually changed from yellowish to dark red within 10 min of the thiol addition. After 12 h of stirring, a red precipitate formed, which was isolated by centrifugation, and it was isolated through repeated washing with methanol and cold water. The resulting Ag₂₁ cluster (synthetic yield of 60%), obtained as a red powder, was used for further studies.

The Ag₄₂ cluster was synthesized using a similar LEIST protocol. In this reaction, 4.2 mg of CBDT-H₂ dissolved in methanol was added to a methanolic solution of the Ag₁₈ nanocluster (≈10 mg). The mixture was stirred thoroughly, initially forming a white precipitate, which gradually transformed into a brownish solid after 5 h of continuous stirring, indicating the formation of the Ag₄₂ cluster. The brown product (yield of 65%) was collected and purified by multiple washings with methanol prior to further studies.

Synthesis of Ag₃₁ Nanocluster: The synthesis was carried out via a TPP-assisted co-reduction of AgNO₃ and TRZ-H₂, following the previously reported procedure.^[69] Briefly, 20 mg of AgNO₃ was dissolved in 5 mL of methanol and mixed with 25 mg of TRZ-H₂ dissolved in 9 mL of DCM.

Subsequently, 45 mg of TPP was added to the mixture. After 20 min of stirring, the resulting solution was reduced by adding 12 mg of NaBH₄ dissolved in 1 mL of ice-cold water. The reaction was allowed to proceed for 6 h, ultimately yielding a purple-colored Ag₃₁ cluster. The dark violet solid (synthetic yield of 75%) was isolated by repeated washings with methanol and hexane and was used for further studies.

Synthesis of Ag₂₂ Nanocluster: In a typical one-pot synthesis reported previously, AgNO₃ (20 mg) was dissolved in MeOH/DCM (5/9 mL, v/v), followed by the addition of 2,5-DMBT (10 μL) and DPPE (10 mg).^[71] After stirring for 15–20 min, NaBH₄ (20 mg) in 1 mL ice-cold water was added dropwise, changing the solution color from yellow to dark brown. 15 mg of PPh₄Cl and a few drops of triethylamine were then introduced, and the reaction was stirred for 12 h under ice-cold conditions. The product was isolated by washing, solvent evaporation, and MeOH extraction, yielding purified nanoclusters soluble in a wide range of organic solvents. Dried powder obtained from a methanol solution was used for further studies.

Synthesis of Ag₄₄ Nanocluster: 20 mg of AgNO₃ was dissolved in DCM/MeOH (10/5 mL, v/v), followed by the addition of 3,4-difluorobenzenethiol (10 μL) and PPh₄Br (15 mg) at 0 °C. After 20 min, NaBH₄ (40–45 mg) and a few drops of triethylamine were introduced, and the reaction was aged for 12 h at 0 °C. The organic phase was washed, and powder of (PPh₄)₄[Ag₄₄(SC₆H₃F₂)₃₀] was obtained upon drying the DCM solution of the cluster.^[72]

Gas-Diffusion Electrode Preparation: The catalyst ink was prepared by dispersing 4 mg of samples in 3 mL of isopropanol and 6 μL of Nafion solution (5% wt.). The prepared solution was sonicated for 30 min. The obtained solution, which was the catalyst ink, was coated on the gas diffusion layer (Sigracet 35BC GDL) using the airbrush method to generate a gas diffusion electrode (GDE). The GDE was then dried at 130 °C for 1 h inside a vacuum oven. The loading was calculated by precisely weighing the GDL before and after applying the catalyst via airbrushing. Catalyst loading was optimized within the range of 0.2–1 mg cm⁻², with 0.5 mg cm⁻² being selected for the eCO₂R tests.

Electrochemical Reduction of CO₂ and Product Analysis: Electrochemical measurements were conducted under dark conditions to minimize the photosensitive behavior of silver clusters. All CO₂ electrochemical reduction tests were performed using a Gamry Interface 1010E potentiostat under the chronoamperometric mode, which applies a constant voltage to a customized flow cell. A 1 M KOH electrolyte was used in the flow cell setup, with Ni foam as the anode and an anion exchange membrane FAA-3-PK-75 as the separator. Utilizing a mass flow controller (Alicat Scientific), a CO₂ gas flow of 50 sccm (standard cubic centimeters per minute) was controlled at the cathode. The electrolyte was supplied to the cell using syringe pumps (New Era Pump Systems Inc.), with flow rates set at 1.0 mL min⁻¹ for the cathode and 2.0 mL min⁻¹ for the anode. The reference electrode used was Ag/AgCl (3 M KCl), which was utilized for determining cathodic potential. All potentials were referenced to the RHE scale using the following conversion equation:

$$E_{RHE} = E_{Ag/AgCl} + 0.209 V + 0.0591 \times pH \quad (1)$$

For product monitoring and gas analysis, an online gas chromatograph (GC, SRI Multiple Gas #5) equipped with a flame ionization detector and thermal conductivity detectors was utilized. To measure the actual CO₂ flow rate at the outlet of the flow cell, an argon gas stream at 10 sccm was mixed with the outlet gas stream from the flow cell before being directed to the GC in a closed loop.

Faradaic Efficiency Calculation:

$$FE (\%) = \frac{zF \times V \times 100\%}{j_{total}} \quad (2)$$

where *z* is the number of electrons required to form the target product, *F* is the Faraday constant (964850), *x* represents the molar fraction of the product relative to CO₂ (determined from GC analysis), *V* is the molar flow rate of CO₂ at the outlet, and *j*_{total} is the total current density.

Turnover Frequency Calculation (TOF):

$$TOF = (j/N/F) / (m/M_{Ag}) \quad (3)$$

where j is the partial current for CO production at a specific potential, N is the number of electrons transferred to generate one molecule of CO, which is 2, and F is the Faraday constant (96485 C mol^{-1}). m represents the mass of Ag active sites in the electrode, calculated as $m_{\text{cat}} \times \omega$ where m_{cat} is the mass of catalyst loaded onto the electrode on GDL and ω is the Ag content in the catalyst (wt.%). Finally, M_{Ag} is the atomic mass of Ag ($107.86 \text{ g mol}^{-1}$).

Supporting Information

Supporting Information is available from the Wiley Online Library or from the author.

Acknowledgements

P.J. and A.J. contributed equally to this work. S.R. acknowledges research support from IIT Kanpur (Project 2024098) and the Chandrakanta Kesavan Centre for Energy Policy and Climate Solutions at IIT Kanpur (Project 2021136H). P.J. acknowledges the IIT Kanpur Institute fellowship (2024). The authors thank Shared Equipment Authority of Rice University and central facilities of IIT Kanpur for infrastructure access. T.P. gratefully acknowledges financial support from the Centre of Excellence on Molecular Materials and Functions under the Institution of Eminence program of IIT Madras. T.P. and T.B. acknowledge joint funding from Department of Science and Technology (DST), India and the Ministry of Education, Youth and Sports (MEYS) at Czech Republic's for bilateral initiatives (DST/INT/Czech/P-16/2020; LTAIN19152). T.P. also acknowledges the Science and Engineering Research Board (SERB), India, for the research grant SPR/2021/000439. Additionally, the authors acknowledge BioRender for offering resources to create graphical schemes (Created in BioRender. Jayan, P. (2025) <https://BioRender.com/00xbqj>).

Conflict of Interest

The authors declare no conflict of interest.

Data Availability Statement

The additional data and analysis has been provided in the supporting information. Data available from the authors upon reasonable request.

Keywords

carborane-thiol, CO, electrochemical CO₂ reduction, faradaic efficiency, silver nanoclusters

Received: April 30, 2025
Revised: October 26, 2025
Published online:

- [1] D. Bagchi, S. Roy, S. Ch. Sarma, S. C. Peter, *Adv. Funct. Mater.* **2022**, 32, 2209023.
[2] S. Roy, Z. Li, Z. Chen, A. C. Mata, P. Kumar, S. Ch. Sarma, I. F. Teixeira, I. F. Silva, G. Gao, N. V. Tarakina, M. G. Kibria, C. V. Singh, J. Wu, P. M. Ajayan, *Adv. Mater.* **2024**, 36, 2300713.

- [3] O. S. Bushuyev, P. De Luna, C. T. Dinh, L. Tao, G. Saur, J. Van De Lagemaat, S. O. Kelley, E. H. Sargent, *Joule* **2018**, 2, 825.
[4] S. Nitopi, E. Bertheussen, S. B. Scott, X. Liu, A. K. Engstfeld, S. Horch, B. Seger, I. E. L. Stephens, K. Chan, C. Hahn, J. K. Nørskov, T. F. Jaramillo, I. Chorkendorff, *Chem. Rev.* **2019**, 119, 7610.
[5] A. Al-Mamoori, A. Krishnamurthy, A. A. Rownaghi, F. Rezaei, *Energy Tech.* **2017**, 5, 834.
[6] T. Wilberforce, A. G. Olabi, E. T. Sayed, K. Elsaid, M. A. Abdelkareem, *Sci. Total Environ.* **2021**, 761, 143203.
[7] B. Dziejarski, R. Krzyżyńska, K. Andersson, *Fuel* **2023**, 342, 127776.
[8] H. Shin, K. U. Hansen, F. Jiao, *Nat. Sustain.* **2021**, 4, 911.
[9] H.-R. Molly Jhong, S. Ma, P. J. Kenis, *Curr. Opin. Chem. Eng.* **2013**, 2, 191.
[10] L. Chi, Y. Zhang, Z. Niu, X. Zhang, Y. Li, T. Zhang, S. Sun, P. Lu, K. Tang, M. Gao, *Angew. Chem. Int. Ed.* **2025**, 64, 202503539.
[11] Z.-Z. Niu, L.-P. Chi, Z.-Z. Wu, P.-P. Yang, M.-H. Fan, M.-R. Gao, *NSO* **2023**, 2, 20220044.
[12] J. Hense, M. Bachmann, L. Polte, N. Von Der Aßen, A. Jupke, *Chem. Ing. Tech.* **2022**, 94, 1524.
[13] B. Molitor, H. Richter, M. E. Martin, R. O. Jensen, A. Juminaga, C. Mihalcea, L. T. Angenent, *Bioresour. Technol.* **2016**, 215, 386.
[14] Y. H. Chan, S. N. F. Syed Abdul Rahman, H. M. Lahuri, A. Khalid, *Environ. Pollut.* **2021**, 278, 116843.
[15] C. George, in *Kirk-Othmer Encyclopedia of Chemical Technology* (Ed.: K. Othmer), Wiley, New York **2001**.
[16] S. Mahajan, S. Jagtap, *Appl. Mater. Today* **2020**, 18, 100483.
[17] T. P. Araújo, A. Shah, C. Mondelli, J. A. Stewart, D. Curulla Ferré, J. Pérez-Ramírez, *Appl. Catal., B* **2021**, 285, 119878.
[18] Z. Li, X. Li, R. Wang, A. C. Mata, C. S. Gerke, S. Xiang, A. Mathur, L. Zhang, D.-Z. Lin, T. Li, K. N. Jayarapu, A. Liu, L. Gupta, A. I. Frenkel, V. S. Thoi, P. M. Ajayan, S. Roy, Y. Liu, Y. Liu, *Nat. Commun.* **2025**, 16, 3206.
[19] D. Roy, A. Pal, T. Pal, *RSC Adv.* **2022**, 12, 12116.
[20] C. McManus, J. Hicks, X. Cui, L. Zhao, G. Frenking, J. M. Goicoechea, S. Aldridge, *Chem. Sci.* **2021**, 12, 13458.
[21] G. Zhang, L. Li, Z.-J. Zhao, T. Wang, J. Gong, *Acc. Mater. Res.* **2023**, 4, 212.
[22] S. Zhao, R. Jin, R. Jin, *ACS Energy Lett.* **2018**, 3, 452.
[23] M. Z. Iqbal, S. Imteyaz, C. Ghanty, S. Sarkar, *J. Indust. Eng. Chem.* **2022**, 113, 15.
[24] D. L. T. Nguyen, H. H. Do, M. T. Nguyen, D.-V. N. Vo, V.-H. Nguyen, C. C. Nguyen, S. Y. Kim, Q. V. Le, *Chem. Eng. Sci.* **2021**, 234, 116403.
[25] Q. Chen, P. Tsiakaras, P. Shen, *Catalysts* **2022**, 12, 1348.
[26] K. Qi, Y. Zhang, J. Li, C. Charmette, M. Ramonda, X. Cui, Y. Wang, Y. Zhang, H. Wu, W. Wang, X. Zhang, D. Voiry, *ACS Nano* **2021**, 15, 7682.
[27] R. Wang, H. Haspel, A. Pustovarenko, A. Dikhtirenko, A. Russkikh, G. Shterk, D. Osadchii, S. Ould-Chikh, M. Ma, W. A. Smith, K. Takanebe, F. Kapteijn, J. Gascon, *ACS Energy Lett.* **2019**, 4, 2024.
[28] S. Liu, H. Tao, L. Zeng, Q. Liu, Z. Xu, Q. Liu, J.-L. Luo, *J. Am. Chem. Soc.* **2017**, 139, 2160.
[29] C. Tricella, M. Muhyuddin, R. Nisticò, S. Tosoni, C. Santoro, *Curr. Opin. Electrochem.* **2025**, 51, 101696.
[30] Y. Y. Birdja, E. Pérez-Gallent, M. C. Figueiredo, A. J. Göttle, F. Calle-Vallejo, M. T. M. Koper, *Nat. Energy* **2019**, 4, 732.
[31] S. Jin, Z. Hao, K. Zhang, Z. Yan, J. Chen, *Angew. Chem.* **2021**, 133, 20795.
[32] M. R. Singh, J. D. Goodpaster, A. Z. Weber, M. Head-Gordon, A. T. Bell, *Proc. Natl. Acad. Sci. USA* **2017**, 114, E8812.
[33] S. Jin, Z. Hao, K. Zhang, Z. Yan, J. Chen, *Angew. Chem.* **2021**, 133, 20795.
[34] L. Zeng, J. Shi, H. Chen, C. Lin, *Energies* **2021**, 14, 2840.
[35] X. Deng, D. Alfonso, T.-D. Nguyen-Phan, D. R. Kauffman, *ACS Catal.* **2022**, 12, 5921.

- [36] X. Zou, A. Li, C. Ma, Z. Gao, B. Zhou, L. Zhu, Z. Huang, *Chem. Eng. J.* **2023**, 468, 143606.
- [37] J. Zeng, W. Zhang, Y. Yang, D. Li, X. Yu, Q. Gao, *ACS Appl. Mater. Interfaces* **2019**, 11, 33074.
- [38] L. Zeng, J. Shi, H. Chen, C. Lin, *Energies* **2021**, 14, 2840.
- [39] I. Chakraborty, T. Pradeep, *Chem. Rev.* **2017**, 117, 8208.
- [40] T. Kawawaki, T. Okada, D. Hirayama, Y. Negishi, *Green Chem.* **2024**, 26, 122.
- [41] Y. Du, H. Sheng, D. Astruc, M. Zhu, *Chem. Rev.* **2020**, 120, 526.
- [42] R. Jin, G. Li, S. Sharma, Y. Li, X. Du, *Chem. Rev.* **2021**, 121, 567.
- [43] M. Neumaier, A. Baksi, P. Weis, E. K. Schneider, P. Chakraborty, H. Hahn, T. Pradeep, M. M. Kappes, *J. Am. Chem. Soc.* **2021**, 143, 6969.
- [44] S. Li, A. V. Nagarajan, Y. Li, D. R. Kauffman, G. Mpourmpakis, R. Jin, *Nanoscale* **2021**, 13, 2333.
- [45] M. F. Matus, H. Häkkinen, *Nat. Rev. Mater.* **2023**, 8, 372.
- [46] S. Li, A. V. Nagarajan, D. R. Alfonso, M. Sun, D. R. Kauffman, G. Mpourmpakis, R. Jin, *Angew. Chem. Int. Ed.* **2021**, 60, 6351.
- [47] F. Lü, H. Bao, Y. Mi, Y. Liu, J. Sun, X. Peng, Y. Qiu, L. Zhuo, X. Liu, J. Luo, *Sustain. Energy Fuels* **2020**, 4, 1012.
- [48] K. Kwak, D. Lee, *Acc. Chem. Res.* **2019**, 52, 12.
- [49] Y. Du, H. Sheng, D. Astruc, M. Zhu, *Chem. Rev.* **2020**, 120, 526.
- [50] H. Qian, M. Zhu, Z. Wu, R. Jin, *Acc. Chem. Res.* **2012**, 45, 1470.
- [51] J. Zhao, A. Ziarati, T. Bürgi, *Angew. Chem. Int. Ed.* **2025**, 137, 202504320.
- [52] D. Yang, J. Wang, Q. Wang, Z. Yuan, Y. Dai, C. Zhou, X. Wan, Q. Zhang, Y. Yang, *ACS Nano* **2022**, 16, 15681.
- [53] V. K. Kulkarni, B. N. Khiarak, S. Takano, S. Malola, E. L. Albright, T. I. Levchenko, M. D. Aloisio, C.-T. Dinh, T. Tsukuda, H. Häkkinen, C. M. Crudden, *J. Am. Chem. Soc.* **2022**, 144, 9000.
- [54] Z.-H. Gao, K. Wei, T. Wu, J. Dong, D. Jiang, S. Sun, L.-S. Wang, *J. Am. Chem. Soc.* **2022**, 144, 5258.
- [55] S. Yuan, R. He, X. Han, J. Wang, Z. Guan, Q. Wang, *Angew. Chem. Int. Ed.* **2021**, 60, 14345.
- [56] V. Yadav, A. Jana, S. Acharya, S. Malola, H. Nagar, A. Sharma, A. R. Kini, S. Antharjanam, J. Machacek, K. N. V. D. Adarsh, T. Base, H. Häkkinen, T. Pradeep, *Nat. Commun.* **2025**, 16, 1197.
- [57] D. R. Kauffman, D. Alfonso, C. Matranga, H. Qian, R. Jin, *J. Am. Chem. Soc.* **2012**, 134, 10237.
- [58] L. Qin, F. Sun, X. Ma, G. Ma, Y. Tang, L. Wang, Q. Tang, R. Jin, Z. Tang, *Angew. Chem. Int. Ed.* **2021**, 60, 26136.
- [59] H. Seong, M. Choi, S. Park, H. Kim, J. Kim, W. Kim, J. S. Yoo, D. Lee, *ACS Energy Lett.* **2022**, 7, 4177.
- [60] J. F. Parker, K. A. Kacprzak, O. Lopez-Acevedo, H. Häkkinen, R. W. Murray, *J. Phys. Chem. C* **2010**, 114, 8276.
- [61] S. Zhao, N. Austin, M. Li, Y. Song, S. D. House, S. Bernhard, J. C. Yang, G. Mpourmpakis, R. Jin, *ACS Catal.* **2018**, 8, 4996.
- [62] G. Deng, H. Yun, M. S. Bootharaju, F. Sun, K. Lee, X. Liu, S. Yoo, Q. Tang, Y. J. Hwang, T. Hyeon, *J. Am. Chem. Soc.* **2023**, 145, 27407.
- [63] R. Guo, R. W. Murray, *J. Am. Chem. Soc.* **2005**, 127, 12140.
- [64] Y.-M. Wang, F.-Q. Yan, Q.-Y. Wang, C.-X. Du, L.-Y. Wang, B. Li, S. Wang, S.-Q. Zang, *Nat. Commun.* **2024**, 15, 1843.
- [65] H. Seong, V. Efremov, G. Park, H. Kim, J. S. Yoo, D. Lee, *Angew. Chem. Int. Ed.* **2021**, 60, 14563.
- [66] S. Li, A. V. Nagarajan, X. Du, Y. Li, Z. Liu, D. R. Kauffman, G. Mpourmpakis, R. Jin, *Angew. Chem. Int. Ed.* **2022**, 61, 202211771.
- [67] M. Zhou, C. Zeng, Y. Chen, S. Zhao, M. Y. Sfeir, M. Zhu, R. Jin, *Nat. Commun.* **2016**, 7, 13240.
- [68] A. Jana, P. M. Unnikrishnan, A. K. Poonia, J. Roy, M. Jash, G. Paramasivam, J. Machacek, K. N. V. D. Adarsh, T. Base, T. Pradeep, *Inorg. Chem.* **2022**, 61, 8593.
- [69] A. Jana, W. A. Dar, S. K. Jana, A. K. Poonia, V. Yadav, J. Roy, S. Chandra, K. N. V. D. Adarsh, R. H. A. Ras, T. Pradeep, *Chem. Mater.* **2023**, 35, 7020.
- [70] A. Jana, M. Jash, A. K. Poonia, G. Paramasivam, M. R. Islam, P. Chakraborty, S. Antharjanam, J. Machacek, S. Ghosh, K. N. V. D. Adarsh, T. Base, T. Pradeep, *ACS Nano* **2021**, 15, 15781.
- [71] E. Khatun, M. Bodiuzzaman, K. S. Sugi, P. Chakraborty, G. Paramasivam, W. A. Dar, T. Ahuja, S. Antharjanam, T. Pradeep, *ACS Nano* **2019**, 13, 5753.
- [72] H. Yang, Y. Wang, H. Huang, L. Gell, L. Lehtovaara, S. Malola, H. Häkkinen, N. Zheng, *Nat. Commun.* **2013**, 4, 2422.
- [73] H. Y. V. Ching, X. Wang, M. He, N. P. Holland, R. Guillot, C. Slim, S. Griveau, H. C. Bertrand, C. Policar, F. Bedioui, M. Fontecave, *Inorg. Chem.* **2017**, 56, 2966.
- [74] A. Lashgari, C. K. Williams, J. L. Glover, Y. Wu, J. Chai, J. Jimmy Jiang, *Chem. A Eur. J.* **2020**, 26, 16774.
- [75] G. Kresse, J. Hafner, *Phys. Rev. B* **1994**, 49, 14251.
- [76] J. P. Perdew, J. A. Chevary, S. H. Vosko, K. A. Jackson, M. R. Pederson, D. J. Singh, C. Fiolhais, *Phys. Rev. B* **1992**, 46, 6671.
- [77] G. Kresse, D. Joubert, *Phys. Rev. B* **1999**, 59, 1758.
- [78] J. K. Nørskov, J. Rossmeisl, A. Logadottir, L. Lindqvist, J. R. Kitchin, T. Bligaard, H. Jónsson, *J. Phys. Chem. B* **2004**, 108, 17886.